Photochemical Transformation of Thifensulfuron-Methyl Herbicide by Natural Clays: A Combined Experimental and Theoretical Approach

El Mountassir El Mouchtari [1,*] **, Lekbira El Mersly** [1] **, Lahoucine Bahsis** [1] **, Hicham Zaitan** [2] **, Mohamed Sarakha** [3] **, Salah Rafqah** [1,*]

[1] Laboratory of Analytical and Molecular Chemistry (LCAM), Department of Chemistry, Polydisciplinary Faculty of Safi, Cadi Ayyad University, Morocco; elmountassirelmouchtari@gmail.com (E.M.E.M); kabira.elmersly@gmail.com (L.E.M.); bahsis.lahoucine@gmail.com (B.L) ; rafqah@gmail.com (S.R.);

[2] Laboratory of Processes, Materials, and Environment, Faculty of Science and Technology, Sidi Mohamed Ben Abdellah University, P.O. Box 2202, Fes; hicham.zaitan@usmba.ac.ma (H.Z.);

[3] Institute of Chemistry Clermont-Ferrand (ICCF), Blaise Pascal University, Clermont-Ferrand (II), P.O. Box 80026, 63177 Aubière Cedex, France; mohamed.sarakha@uca.fr (M.S.);

* Correspondence: elmountassirelmouchtari@gmail.com (E.M.E.M); Rafqah@gmail.com (S.R.);

Abstract: This study aims to investigate the behavior of the sorption process and the photolysis reactions of thifensulfuron-methyl (TFSM) on two raw natural clays (kaolinite and montmorillonite). The results show that the Freundlich model best fits all adsorption data and that montmorillonite has considerable adsorption capacity. Concerning the photodegradation of TFSM, the rate constants of a pseudo-first-order reaction can be obtained, and their values are, respectively, 0.206 h^{-1} and 0.107 h^{-1}. The photoproducts found have been identified by Liquid chromatography-mass spectrometry (LC-MS). They are obtained by cleavage of the Sulfonylurea bridge and hydroxylation of the -OCH$_3$ group involving hydroxyl radical formed on the surface of the irradiated clays. Moreover, the adsorption mechanism of TFSM on natural clays was performed through the density functional theory method (DFT) and non-covalent interaction (NCI) analysis, and their photolysis was predicted using local DFT descriptors and the Wiberg bond index. The DFT calculations agreed with the experimental results, making this study better understand the photolysis mechanisms of thifensulfuron-methyl (TFSM).

Keywords: thifensulfuron-methyl; photodegradation; density functional theory; non-covalent interaction analysis; hydroxyl radical; clay, pesticide.

1. Introduction

In recent years, Agricultural activities have produced pesticide contamination of various aquatic ecosystems due to the high annual consumption [1,2]. Nevertheless, they are usually at the center of health and safety considerations due to their toxicity or potential adverse influence on the environment [3]. Thifensulfuron-methyl is a sulfonylurea herbicide used to control grain crops such as rice, corn, and wheat. Thifensulfuron-methyl may filter into surface and groundwater because of its great water solubility, mobility, and persistence [4].

The photodegradation and adsorption of organic pollutants on the soil's surface are affected by many environmental factors, including soil type, soil moisture, and soil properties such as organic and mineral species [5,6]. Clay minerals are generally considered one class of

the most chemically active components of soils. Various clay minerals have shown a great capability of adsorbing organic compounds such as pesticides [7,8]. Several studies have also proven that sunlight photodegradation on the soil surface is an important degradation pathway for a variety of organic pollutants, suggesting the potential importance of clays in soils and subsoil [9–11].

Montmorillonite (MMT), kaolinite (KAO), vermiculite, etc., are natural clay constituents of soils that have a high adsorption capacity due to their low cost, availability, high specific surface area, cation exchange capacity (CEC), good removal efficiency and selectivity, have recently been proposed for remediate soil or water environments [12–14].

Elements metals exist in the environment as oxides, hydroxides, sulfides, or ionic species intercalated in clay. Iron is one of the most abundant transition metals in soil and is considered to play a large role in photoinduced redox reactions [15]. The structural Fe in natural clays is active in the photodegradation of various pollutants, such as nitroaromatic [16], 1,4-dioxane [17], and diethyl phthalate [18]. Other pollutants can form the complex with iron present in the clay, reducing Fe^{3+} to Fe^{2+}, which can start the decomposition of H_2O_2 to produce $°OH$ [19–21]. The mineral clays have been used as TiO_2 support to obtain a better photocatalytic activity and a good separation of the catalyst in water treatment [22–25].

The original crystal structure of MMT and kaolinite was constructed according to experimental data [26,27]. The clay unit cell was optimized using the Dmol3 program package [28]implemented in Accelrys Materials Studio 8.0 [29]. GGA-PBE was selected as the exchange-correlation functional [30] due to its more accurate description of the hydrogen bond [31]. To represent the MMT and kaolinite surfaces in the gas phase, a periodically repeated slab was constructed by cleaving the bulk unit cell at the (001) plane because it is reported that it is the most predominant plane for MMT and kaolinite clays. The surfaces were next enlarged to an (8×9×1) supercell to provide a large surface for the interaction of all components, and then a 30 Å thick vacuum layer was added over the surface to form a flat plate model.

The Monte Carlo (MC) simulation was adopted to compute the low configuration adsorption energy of the TFSM interacting with MMT and kaolinite surfaces, using the Adsorption Locator module [32], and the universal force field (UFF) has been successfully used in the study [33]. The number of cycles was 10, with each cycle of 105 steps. The configurations that result from one of these steps are accepted according to the selection rules of the Metropolis Monte Carlo method [34]. The van der Waals force was calculated using the Atom basis summation method [35], while the static action was calculated using the Ewald & Group summation method [36]. For the aqueous phase study, 100 or 500 water molecules were added to the simulation box. The low-energy adsorption site is identified by a Monte Carlo search for the configurational space of the substrate-adsorbate system (simulated annealing).

DFT calculations are an efficient tool that can provide a closer understanding of the adsorption mechanisms of organic pollutants on clay surfaces. For example, the adsorption of 2,4-dinitrotoluene and cellobiose on kaolinite surfaces [37,38], sulfonamides on phyllosilicate [39], surfactants on montmorillonite [40], neomycin on montmorillonite, sepiolite [41], or to study the interaction of ethambutol with palygorskite [42]. Moreover, the DFT calculations have achieved results of great relevance in the understanding of the mechanisms and kinetics of the photodegradation of organic pollutants, for example; the DFT approach investigated the rate constants between •OH and eight organic pollutants, and the estimated values were within a factor of 5 of the experimental values [43]. The radical oxidation (•OH) pathways of organic pollutants were also studied by DFT calculations by the construction of the energy profiles for

these reaction channels, which can explain the experimental evidence obtained[44–47]. In the present work, two commercial clays, kaolinite and montmorillonite, representative natural minerals clays, were used as support to investigate the effect composition on the adsorption and photodegradation of the pesticide thifensulfuron-methyl (TFSM). In addition, a DFT calculation was performed to understand the adsorption and photolysis of TFSM molecules on kaolinite and montmorillonite surfaces.

2. Materials and methods

2.1. Reagents and materials.

Thifensulfuron-methyl: methyl 3-[[(4-methoxy-6-methyl-1,3,5-triazin-2yl)carbamoyl] sulfamoyl] -2- thiophene carboxylate (TFSM) (purity 99.9%) was obtained from Riedel-de Haëen and used as received.

The characteristic UV–Visible absorption spectra of TFSM and solar emission spectrum are shown in Figure 1.
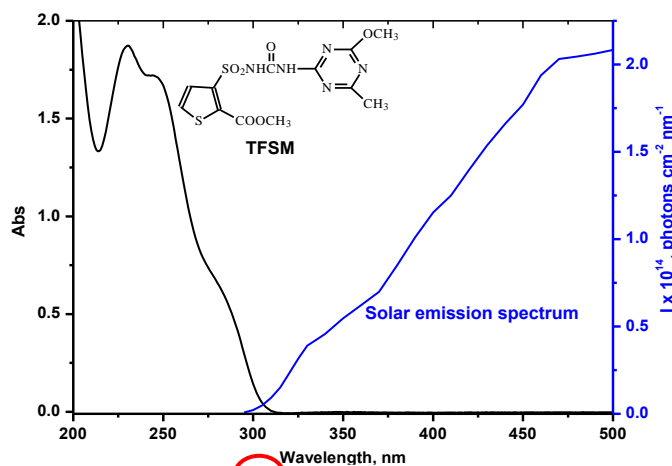

Figure 1. Characteristic UV–Visible spectra of TFSM (1.0×10^{-4} mol.L^{-1}) in aqueous solution and solar emission spectrum.

Montmorillonite-K(MMT) and Kaolinite (KAO) were purchased from Aldrich Chemical Co. The chemical composition of the MMT and KAO samples is presented in Table 1.

Table 1. Chemical composition of MMT and KAO samples.

Oxide (%)	(MMT)	(KAO)
SiO$_2$	71,47	45,41
Al$_2$O$_3$	14,36	35,06
Fe$_2$O$_3$	**2,99**	**0,65**
MnO	0,017	0,013
MgO	1,41	0,21
CaO	0,21	0,05
Na$_2$O	0,37	0,13
K$_2$O	1,72	1,45
TiO$_2$	**0,52**	**0,054**
P$_2$O$_5$	0,048	0,11

2.2. Adsorption.

Adsorption isotherm studies of the pesticide on clay samples were performed using the batch method of the following technique: 10 mL of Thifensulfuron-methyl solution of desired

initial pesticide concentrations (0 to 2.0×10^{-4} mol.L^{-1}) was added into 50 mg clay in a 60 mL brown bottle with a plug. The suspensions were agitated on a shaker for 24 h at 22 ±1°C to achieve equilibrium.

After that, the solid phase was separated from the solution by centrifugation at 4000 rpm for 15 min. Finally, the supernatant was decanted and passed through a 0.45 µm Millipore syringe filter.

The adsorption isotherm is fundamental for understanding the mechanism of adsorption. Important information regarding how the adsorbate molecules distribute between the liquid and solid phases once the equilibrium state is reached can be interpreted based on the adsorption isotherm.

Its adsorption isotherms were derived based on batch analysis to investigate the adsorption processes of the clays used in the pesticide studied. In this study, the Freundlich model based on a sum of least squares analysis best fits all adsorption data. The Freundlich model has the following form:

$$C_s = K_f \, C_e^n$$

(Eq.1)

where Cs is the adsorbed pesticide per mass unit sorbent (mg/kg), Ce is the equilibrium concentration of the pesticide (mg/L), and Kf (mg/kg) (mg/L)-n and n (dimensionless) are constants at a given temperature.

Eq.(1) can be linearized by a logarithmic transformation:

$$\log C_s = \log K_f + n \log C_e$$

(Eq.2)

If Eq. (1) is applicable, a plot of log(Cs) vs. log(Ce) gives a straight line with the slope n and the intercepted log(Kf).

2.3. Irradiation experiments.

Photodegradation experiments were carried out on clay samples exposed to Suntest (300-600 nm) at different times and then extracted from each irradiated sample methanol (1 mL), filtered through a 0.45 µm Millipore syringe filter. The procedure was repeated for all clay complexes prepared.

2.4. Experimental procedure and analyses.

The Thifensulfuron-methyl was determined qualitatively and quantitatively through high-performance liquid chromatography using a Waters 540 HPLC chromatography system equipped with a Waters 996 photodiode array detector (DAD). The experiments were performed by UV detection at either 250 nm or using a reverse-phase Nucleodur column (C18-5µm; 250–4.6 mm). The flow rate was 1.0 mL min^{-1}, and the injected volume was 50µL. The elution was accomplished with water, acetic acid (0.1%), and acetonitrile (60/40, v/v).

The degradation of THFS was accompanied by the formation of several byproducts, which were identified by HPLC electrospray tandem mass spectrometry (LC/MS).

LC/MS studies were carried out with a Waters (Alliance 2695) HPLC system coupled to a Quattro LC triple quadrupole mass spectrometer (Micromass, Manchester, UK) equipped with a pneumatically assisted electrospray ionization source (ESI). Data acquisition and processing were performed by the Mass Lynx NT 3.5 system. Chromatography was run using a Kinetex MS C18, 2.6 µm, 100 mm × 2.1 mm and a 6/4 v/v mixture of acetonitrile and water with 0.2 % acetic acid as mobile phase at 0.2 mL min^{-1}. The electrospray source parameters

were: capillary voltage of 3.5 kV (or 3 kV in the negative mode), cone voltage of 15 V, source block temperature of 120°C, and desolvation gas temperature of 400°C. Argon was used for collisionally activated dissociation (CAD) at a pressure of 1.5 10^{-3} torr and 10-50 eV collision energy. The UV-visible absorption spectra measurements were acquired on a Cary 3 double-beam UV-Vis (Varian) with a 1 cm quartz cuvette over the 200-800 nm range.

2.5. Computational details.

2.5.1. Geometry optimization.

The geometry optimization of thifensulfuron-methyl (TFSM) was performed using the DFT method. The DFT calculations were carried out with the GAUSSIAN 09 [48] by using the exchange-correlation functional B3LYP [49,50]and 6-311G (d, p) basis set. Frequency calculations were executed to verify the stationary points to be real minima at the same level. Furthermore, all charge distributions were calculated by Natural Bond Orbital (NBO) analysis [51].

2.5.2. Reactivity descriptors.

The Fukui function was used to predict the degradation mechanism of the optimized TFSM molecule. Fukui function is based on the conceptual density functional theory (CDFT) [52], which showed that sites in chemical species with the largest values of f(r) are those with higher reactivity. The Fukui function was defined as:

$$f_k = \left[\frac{\partial \rho(r)}{\partial N}\right]_{v\,(r)} \qquad (Eq.3)$$

where N is the number of electrons, $\rho(r)$ is the electronic density and the constant term v in the partial derivative is the external potential. However, the electron density of a neutral or $N_{0\pm electron}$ molecule contains all the information that reflects the reactivity of a site of a molecule. Most studies in the literature have been carried out in the so-called finite difference method [53], in which the Fukui functions f (r) are approximated as:

$f_k^- = [q_k(N) - q_k(N - 1)]$ for electrophilic attacks

$f_k^+ = [q_k(N+1) - q_k(N)]$ for nucleophilic attacks

$f_k^0 = \frac{1}{2}*[f_k^- + f_k^+]$ for radical attacks

where q(N), q(N+1), and q(N-1) are the charges at atom k on the neutral, anionic, and cationic species, respectively. Moreover, the local softness s(r) is more important than Fukui functions when comparing different sites in different molecules [54]. The latter is related to local softness through s(r) = Sf(r), indicating that f(r) redistributes the global softness among different parts of the molecule [55,56].

2.6. Non-covalent interactions (NCI) analysis.

The non-covalent interaction (NCI) analysis was also carried out on the most stable structure of TFSM on surface clays. The NCIs analysis evaluates the intermolecular interactions and can be revealed solely through the reduced density gradient, s, which is a scalar field of the electron density (ρ) and can be defined as :

$$S = \frac{|\nabla\rho|}{2(3\pi^2)\rho^{4/3}} \qquad (Eq.4)$$

The S function has higher values in regions outside the molecule and lower values near the covalent bonds and non-covalent interactions, which appear as peaks in the s (ρ) diagram

[57]. The limiting interaction cases like hydrogen bonds, van der Waals, and steric repulsions are reflected here with a coloring scheme (blue, green, and red, respectively). Multiwfn [58]conducted the non-covalent interactions, and their visualization was done with Visual Molecular Dynamics VMD [59].

3. Results and discussion

3.1. Chemical analysis.

Table 1 regroups the chemical composition of the two clays utilized**.** It was observed that this clay is rich in SiO_2 (71.4% MMT, 45.4% KAO), Al_2O_3 (14.3% MMT, 35.06% KAO), Fe_2O_3 (2.99% MMT, 0.65% KAO), K_2O (1.72% MMT, 1.45% KAO) and TiO_2 (0.52% MMT, 0.05% KAO). Some other elements exist but in small percentages. The percentage of Fe_2O_3 and TiO2 allows this clay to be used in photocatalytic processes.

3.2. Adsorption isotherm of Thifensulfuron-methyl.

The parameters of the Freundlich equation for the adsorption of pesticide onto the clays obtained as described above are presented in Table 1, together with experimental data points (calculated by fitting Eq. 4). The fit of experimental isotherm data to the Freundlich equation confirms to be quite good when correlation coefficients R2 obtained from linear regression analysis are examined.

The two values of n calculated for the adsorption of this pesticide onto different used clays were similar from one sample to another with n~1.0. Still, the value of Kf for the montmorillonite was greater than that for Kaolinite-based clay. It was expected that these clay minerals of the montmorillonite group with larger specific surface area (Table 3), could adsorb the pesticide studied in each layer. A similar study showed that montmorillonite has considerable adsorption capacity because of its large surface area [59].

This surface area was not the only factor contributing to the high adsorption of thifensulfuron methyl (TFSM). Another factor that can control adsorption is the value of the cation exchange capacity. Montmorillonite has a very high CEC compared to kaolinite; the values obtained being 5.83 meq/100g (kaolinite) and 60.68 meq/100g (montmorillonite) (Table 3), which are consistent with those reported in the literature [60]. Therefore, increasing the CEC value results in an increase in the rate of adsorption [61].

Table 2. Values of K_f and n for the Freundlich Equation for the adsorption of thifensulfuron-methyl on used clays.

	n	K_f	R^2
MMT- TFSM	0.747	33.27	0.98
K- TFSM	0.884	2.37	0.97

Table 3. Values of the cation exchange capacity and the specific surface area of (MM) and (KOA).

Clay	(MMT)	(KAO)
CEC (meq/100)	60,68	5,83
S_{BET} ($m^2.g^{-1}$)	166	5

3.3. Photodegradation kinetics of thifensulfuron-methyl.

The influence of UV irradiation was first studied. One can see that Thifensulfuron-methyl could be transformed by UV light on the solid support. From the results shown in Figure 2, the rate constants of a pseudo-first-order reaction can be obtained. The rate constants for

TFSM/montmorillonite and TFSM/Kaolinite under UV light irradiation are 0.206 h^{-1} and 0.107 h^{-1}, respectively. Since they may be involved as photoinduced, some inorganic species in soil. It has to be taken into account that they can present an accelerating effect on degradation reactions such as Fe_2O_3 and TiO_2.
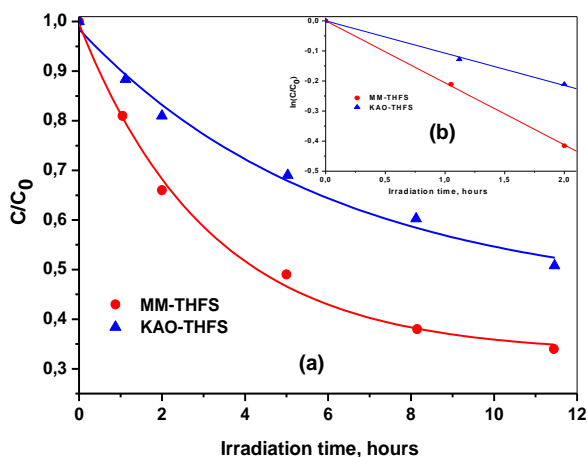

Figure 2. Photodegradation kinetics of Thifensulfuron-methyl on (**A**) kaolinite and (**B**) montmorillonite surface under UV light and the effect of the adsorbed species.

3.4. Photoproducts elucidation and mechanism.

Photoproducts generated after irradiation of thifensulfuron-methylonto the montmorillonite and kaolinite were identified by using LC-MS with electrospray ionization in negative as well as positive modes (Figure 3). Photoproduct was easily identified as 2-amino-4-methoxy-6-methyl-1,3,5-triazine (AMMT). This identification was based on the comparison with an authentic sample. The compound is obtained by the photohydrolysis of the sulfonylurea link, and it is a typical degradation pathway of sulfonylurea herbicides under irradiation.
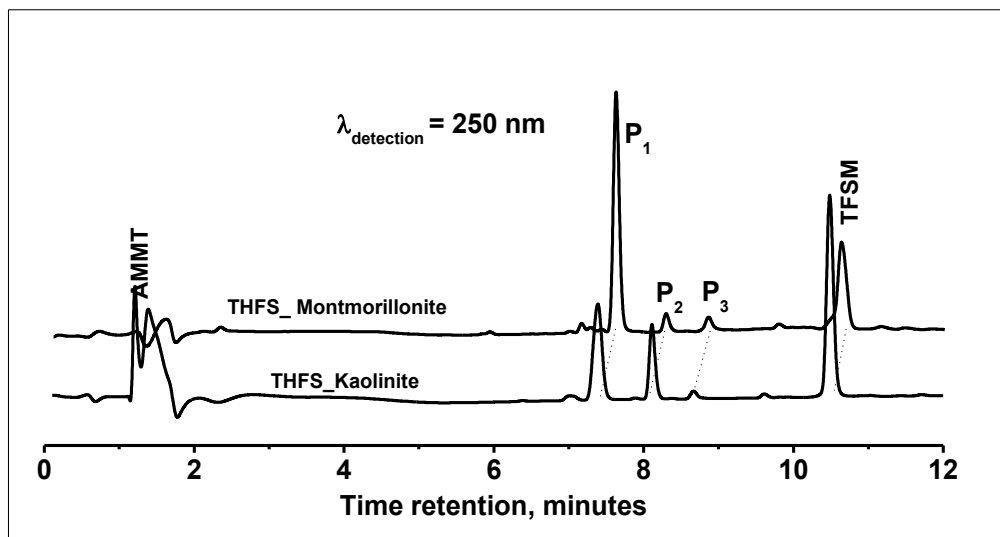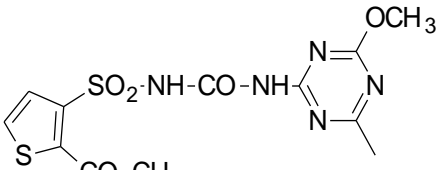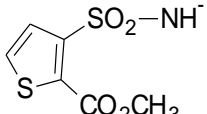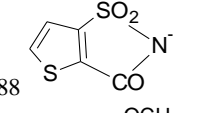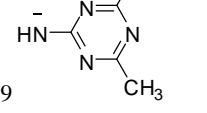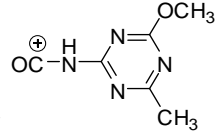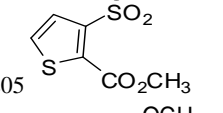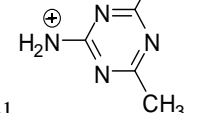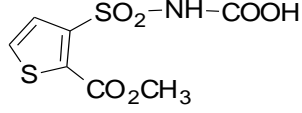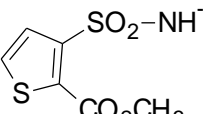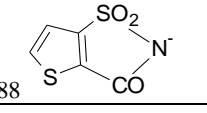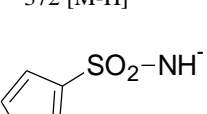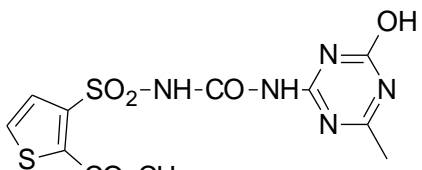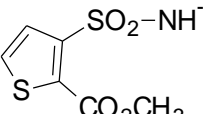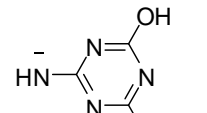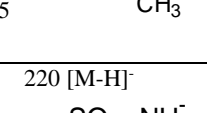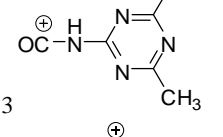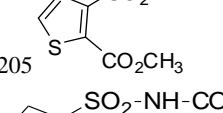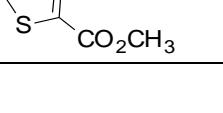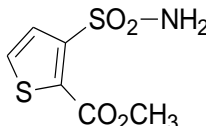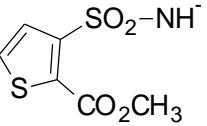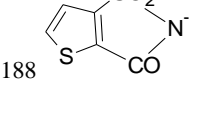

Figure 3. HPLC chromatogram of a solution obtained by extraction with methanol of an irradiated mixture of TFSM/Kaolinite and TFSM/ Montmorillonite.

A mass spectrometry characterization of TFSM was previously carried out to optimize the conditions of the instrumental sensitivity of mass spectrometry analysis and to build a fragmentation pattern that could be useful for the identification of the photoproducts.

The results obtained are shown in Table 4.

Table 4. m/z values and products ion from LC-mass (ESI- and ESI+) of thifensulfuron-methyl photoproducts.

Product	Observed m/z and structure ion	
Thifensulfuron-methyl (387g/mol) t=10.5 mn — structure: thiophene ring with SO₂-NH-CO-NH-triazine(OCH₃)(CH₃), CO₂CH₃	386 [M-H]⁻ — 220 (SO₂-NH⁻ / CO₂CH₃ thiophene); 188 (thiophene SO₂-N⁻-CO); 139 (HN-triazine OCH₃, CH₃)	388 [M+H]⁺, 410 [M+Na]⁺ — 167 (OC-N⁺H-triazine OCH₃, CH₃); 205 (thiophene SO₂⁺, CO₂CH₃); 141 (H₂N⁺-triazine OCH₃, CH₃)
P1 (264 g/mol) t = 7.2 mn — structure: thiophene SO₂-NH-COOH, CO₂CH₃	263 [M-H]⁻ — 220 (thiophene SO₂-NH⁻, CO₂CH₃); 188 (thiophene SO₂-N⁻-CO)	
P2 (373 g/mol) t= 7.8 mn — structure: thiophene SO₂-NH-CO-NH-triazine(OH)(CH₃), CO₂CH₃	372 [M-H]⁻ — 220 (thiophene SO₂-NH⁻, CO₂CH₃); 125 (HN-triazine OH, CH₃)	374 [M+H]⁺ — 153 (OC-N⁺H-triazine OH, CH₃); 205 (thiophene SO₂⁺, CO₂CH₃); 248 (thiophene SO₂-NH-CO⁺, CO₂CH₃)
P3 (220 g/mol) t=8.5 mn — structure: thiophene SO₂-NH₂, CO₂CH₃	220 [M-H]⁻ — 188 (thiophene SO₂-N⁻-CO); (SO₂-NH⁻, CO₂CH₃)	

Several studies proposed the mechanism of sulfonylurea degradation by simulated sunlight in water and on a soil surface. The major photolysis reaction is the homolytic cleavage of one of the bonds of the sulfonylurea bridge. Still, the nature of the final products depends on the substituent of the molecular. The cleavage of the S–N bond was observed as the main pathway for this family of pesticides. For chlorsulfuron [62,63], bond cleavage of the C–S is the main photochemical pathway for some sulfonylurea as triasulfuron, cinosulfuron [64], and metsulfuron-methyl [15,65]. Concerning the scission of the C-N bond, it was recognized as the main pathway for tribenuron methyl [66]. Some other photochemical reactions involved the two rings, aromatic and triazinic.

In our experimental conditions, the photodegradation of thifensulfuron-methyl on kaolinite and montmorillonite surfaces allowed the formation of four photo products. They were obtained following two types of reactivity: by rupture of the sulfonylurea bridge and by hydroxylation. The byproducts implying the sulfonylurea bridge are obtained from the homolytic scission of bond β(C-H), eventually forming the products P3 and AMMT *(pathways 2)*. Also, photohydrolysis and/or attack by radicals $^{\bullet}$OH on the bond α(C-H) can generate the products P1 and AMMT (pathways 1 and 4). This type of reaction was observed by [67]. However, the product P2 was observed by hydroxylation of the group (OCH3) (pathways 2). Indeed, hydroxyl radicals can be formed on the surface of kaolinite and montmorillonite via two processes. (i) The involvement of TiO_2 and Fe_2O_3, which are part of the composition of the two clays, are known by their photocatalytic effect in several studies. (ii) The photoinduced behavior of some types of clays according to the reactions presented below[68–70]:

$$Clay + O_2 \xrightarrow{h\nu} Clay^{\overset{\bullet}{+}} + O_2^{\overset{\bullet}{-}}$$

$$O_2^{\overset{\bullet}{-}} + H_2O \longrightarrow OH_2^{\overset{\bullet}{-}} + OH^-$$

$$OH_2^{\overset{\bullet}{-}} + H_2O \longrightarrow H_2O_2 + HO^{\bullet}$$
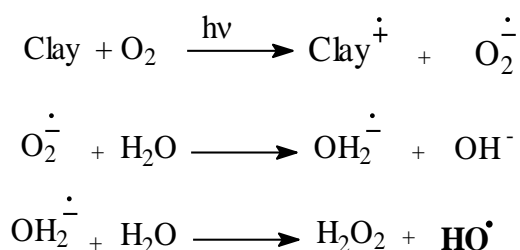
Figure 4 presents the possible mechanism of photodegradation of Thifensulfuron-methyl on the montmorillonite and kaolinite.
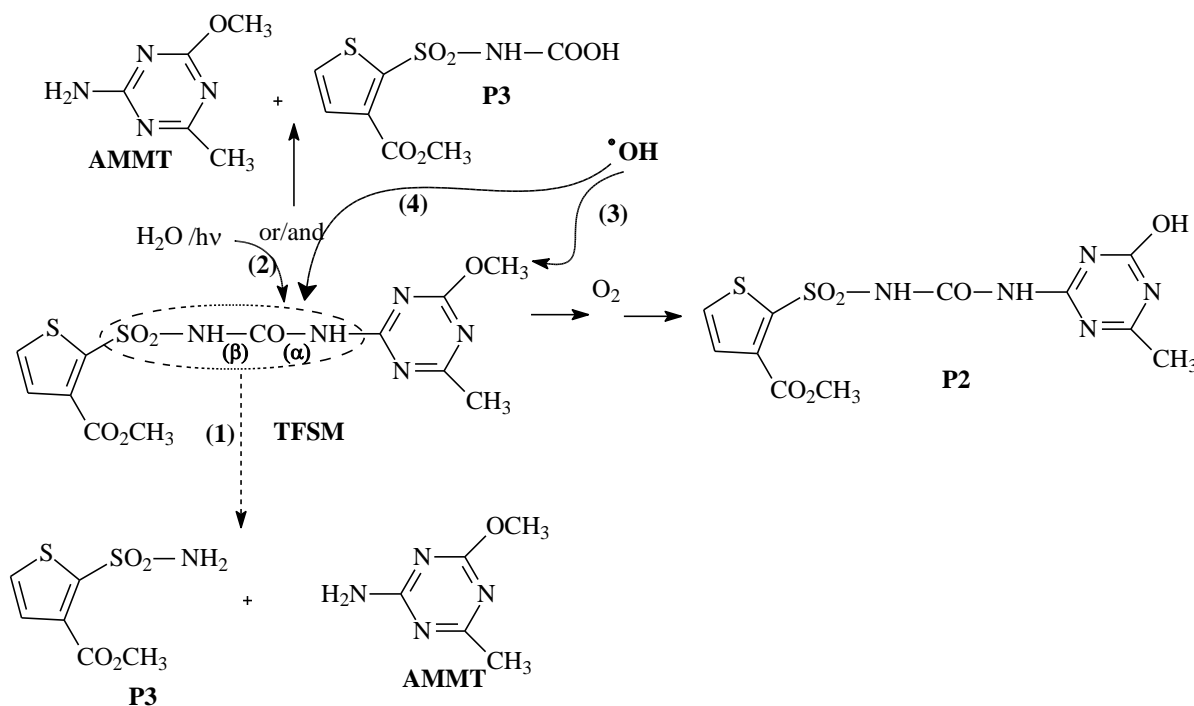
Figure 4. Photoproducts and proposed pathways of thifensulfuron-methyl on montmorillonite and kaolinite surface.

3.5. *Mechanism of TFSM adsorption on MMT and kaolinite surfaces.*

The adsorption mechanism of thifensulfuron-methyl (TFSM) onto two natural clays (kaolinite and montmorillonite) was investigated using Monte Carlo (MC) simulations. The close contacts between the TFSM molecule and the surface of the clay as well as the best adsorption configuration for the compound, are presented in Figures 5 and 6. In gas and aqueous phases, the interactions between TFSM and natural clays occur via several lone-pair

electrons containing N, O, and S atoms and π-aromatic systems. The more stable configurations of FTSM adsorption on the MMT (001) and kaolinite (001) were obtained using the MC method, and the results in gas and water phases were listed in Table 5. The adsorption configurations of the title compound in the gas phase were -156.61 and -152.12 kcal/mol on the MMT and kaolinite surfaces, respectively (Figure 5). Interestingly, adding water makes the adsorption of TFSM on MMT more stable (E_{ads}= -2.12 10^3 kcal/mol), where their adsorption energy in kaolinite is -2.05 10^3 kcal/mol (Figure 6). These results explained the considerable adsorption capacity of MMT compared with kaolinite surfaces in the aqueous medium.
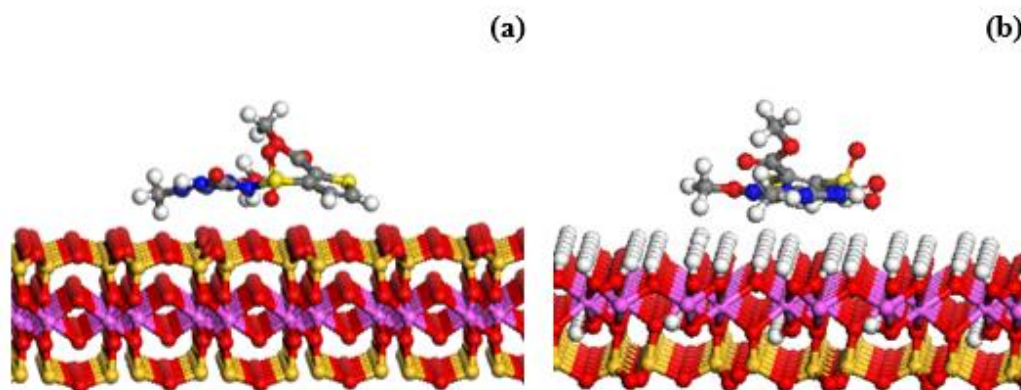
Figure-5. The most stable low-energy configuration for the adsorption of TFSM on **(a)** MMT (001) and **(b)** kaolinite (001) surfaces in the gas phase obtained using the Monte Carlo simulation.

Table 5. Adsorption energies (E_{ads}) for TFSM on MMT (001) and kaolinite (001) surfaces in gas and aqueous phases were obtained using the Monte Carlo simulation (in kcal/mol).

	Gas	Aqueous (100 H$_2$O)	Aqueous (500 H$_2$O)
MMT (001)	-156.61	-579.76	-2.13 10^3
Kaolinite (001)	-152.12	-548.83	-2.05 10^3

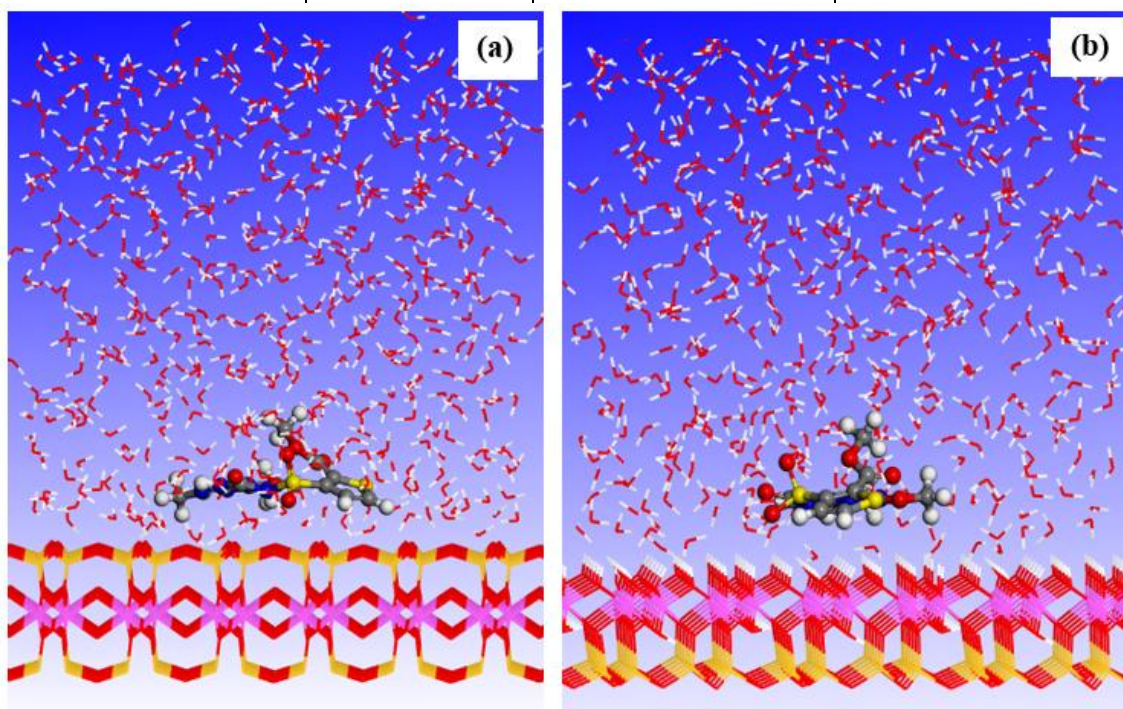**Figure-6.** The most stable low-energy configuration for the adsorption of TFSM on **(a)** MMT (001)/500H$_2$O and **(b)** kaolinite (001)/500H$_2$O systems obtained using the Monte Carlo simulation.

The interactions of the TFSM molecule in the gas phase with MMT and kaolinite surfaces and their cooperative interactions were further demonstrated with non-covalent

interactions (NCI). The NCI isosurfaces for TFSM adsorbed on the MMT and kaolinite surfaces are displayed in Fig-7. The green region between the title compound and clay surfaces suggests that the weak vdW interaction has a key role in the adsorption of TFSM by clays. The vdW interaction results via X-π (X: N, O, and S atoms) interactions for the MMT surface and X-H (X: N and O atoms) interactions for kaolinite, occurring via the 1,3,5-triazine, thiophene rings, and SO_2 group. Moreover, moderate steric repulsion can also be observed as well based near the red region, displayed by repulsive interactions in TFSM and Si-Si interactions on the MMT surface.
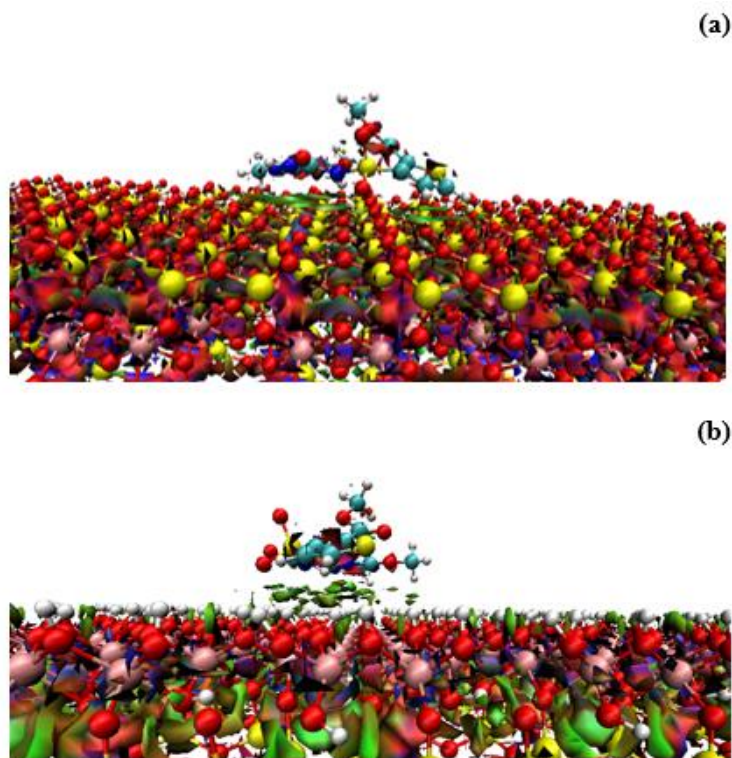

Figure 7. Gradient isosurfaces (s = 0.5 au) for TFSM intercalated and covalently grafted **(a)** MMT and **(b)** kaolinite surfaces (Al, coral; O, red; C, cyan; Si, yellow; H, white). Blue, green, and red circles represent hydrogen (H)-bond, Van der Waals (vdW), and steric repulsive interactions.

3.6. Theoretical prediction of degradation mechanism.

To explain the photodegradation reaction of TFSM on surface clays, the "softness-matching principle" was applied, indicating that the interaction between two chemical species will occur through the atoms whose softnesses are approximately equal [71]. Based on this, Δs^0 between the reacting atoms must be as small as possible. Therefore, $\Delta s^0 = s^0(O) - s^0(X)$, the difference between the local softnesses of the oxygen atom of the attacking •OH radical and the atom (X) of the TFSM molecule were calculated for each of the atoms of the molecule. The calculated Fukui functions f^0, local softness s^0, and softness difference Δs^0 are presented in Table 6.

Since S9 and C19 atoms with the highest f^0 are the first sites where the •OH radical attack will occur, their products were identified in previous studies (Figure 8) [72]. These reactions were not observed using MMT and kaolinite surfaces. The local softness s^0 and softness difference Δs^0 values indicate that the C6 atom is the next target of hydroxyl radical attack. The results indicate that C6-N4 bond cleavage takes place, resulting in the formation of intermediate P1 (Figure 8). Then, intermediate P1 upon the attack of the •OH radical and the formation of CO_2 groups. The chemical reactivity indices in Table 6 imply that •OH radical

attacks first C6 and N4 atoms, then N7, yielding intermediates P3 and AMMT compounds. In addition, •OH radical attacks the C30 atom on the triazine ring and yields compound P2 by the removal of -OCH$_3$ groups. All these findings were in good agreement with the experiment results, and the compounds formed were detected by the LC-MS technique.

Table 6. Chemical reactivity descriptors for TFSM and the •OH radical.

|	TFSM (S=10.7694)		
	f^0	s^0	Δs^0
C1	0.0003	0.0031	3.1979
C2	0.0014	0.0155	3.1855
C3	0.0053	0.0570	3.1440
N4	-0.0025	-0.0268	3.2278
H5	-0.0093	-0.1003	3.3013
C6	0.0105	0.1132	3.0878
N7	-0.0386	-0.4154	3.6164
H8	-0.0069	-0.0741	3.2751
S9	0.0340	0.3662	2.8413
C10	-0.0213	-0.2292	3.4302
C11	-0.0031	-0.0332	3.2342
O12	-0.1454	-1.5660	4.7670
O13	-0.1244	-1.3402	4.5412
O14	-0.0477	-0.5141	3.7151
C15	-0.0227	-0.2448	3.4458
N16	-0.0436	-0.4700	3.6710
N17	-0.0487	-0.5250	3.7260
N18	-0.0190	-0.2051	3.4061
C19	0.0112	0.1207	3.0803
O20	-0.0106	-0.1145	3.3155
O21	0.0019	0.0201	3.1809
C22	0.0029	0.0312	3.1698
H23	-0.0068	-0.0732	3.2742
H24	-0.0088	-0.0944	3.2954
H25	-0.0041	-0.0442	3.2452
H26	-0.0137	-0.1478	3.3488
C27	-0.0126	-0.1353	3.3363
S28	-0.0266	-0.2869	3.4879
O29	-0.0001	-0.0013	3.2023
C30	0.0029	0.0314	3.1696
H31	-0.0051	-0.0548	3.2558
H32	-0.0046	-0.0491	3.2501
H33	-0.0049	-0.0527	3.2537
C34	0.0010	0.0104	3.1906
H35	-0.0069	-0.0739	3.2749
H36	-0.0067	-0.0720	3.2730
H37	-0.0060	-0.0647	3.2657
H38	-0.0090	-0.0972	3.2982
OH radical (S = 4.1234)			
O	0.7736	3.2075	
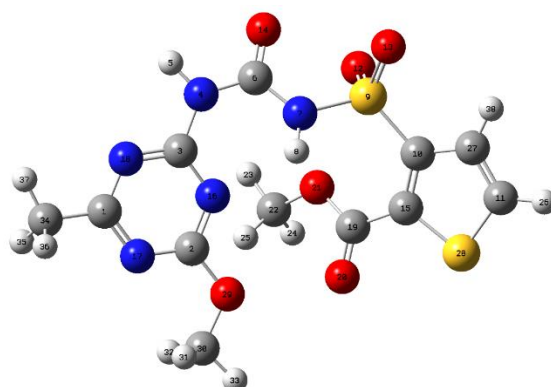
Figure 8. Optimized structure of TFSM and the numbering system (C, grey; O, red; N, blue; H, white; S, yellow).

Wiberg bond indexes (WBI) were calculated for TFSM molecules to determine the strength of a given chemical bond [73]. The lowest excited triplet state was found to be long-lived photochemical reaction precursors for many compounds and reactions of an excited molecule [74,75]. For this, the geometry of TFSM was investigated at its triplet states with a spin multiplicity of 3, and the results were reported in Table 5. The WBI index of S9-N7, N7-C6, and C6-N4 bonds of the TFSM are about 0.75, 1.10, and 1.00 for singlet and 0.18, 0.27, and 0.25 for triplet (Table-5). This indicates that these bonds in the excited state are significantly weakened, thus resulting in its feasible decomposition by photolysis. The LUMO-HOMO energy gap of TFSM is about 0.18 a.u. for singlet and less than 0.09 a.u. for triplet, indicating an increase in the reactivity of this molecule at the triplet state (Table-5). Therefore, the C6-N7 and C6-N4 bonds could be more reactive in the triplet than the singlet state. With all these in mind, the decrease in WBI and smaller LUMO-HOMO energy gap could account for the higher reactivity of the C6-N bond in the exciting TFSM molecule.

Conclusions

The adsorption capacity and photodegradation activity were tested on Thifensulfuron-methyl, using kaolinite and montmorillonite as support. The maximum adsorption capacity and photodegradation were observed for the second clay. The photoproducts were identified using the LC-MS technique, which allowed us to propose a photodegradation mechanism. Moreover, the theoretical results were in good agreement with the experimental results, which makes this study a new way to understand the photolysis mechanisms of thifensulfuron-methyl (TFSM).

Conflicts of interest

On behalf of all authors, the corresponding author states that there is no conflict of interest.

Acknowledgment

Funding

References

1. Serasinghe, P.; Nguyen, H.T.K.; De Silva, T.; Nugegoda, D.; Pettigrove, V. A Novel Approach for Tailoring Pesticide Screens for Monitoring Regional Aquatic Ecosystems. *Environmental Advances* **2022**, *9*, 100277, https://doi.org/10.1016/j.envadv.2022.100277.
2. Fuchte, H.E.; Beck, N.; Bieg, E.; Bayer, V.J.; Achten, C.; Krauss, M.; Schäffer, A.; Smith, K.E.C. A Look down the Drain: Identification of Dissolved and Particle Bound Organic Pollutants in Urban Runoff Waters and Sediments. *Environmental Pollution* **2022**, *302*, 119047, https://doi.org/10.1016/j.envpol.2022.119047.
3. Vega, D.; Cambon, J.-P.; Bastide, J. Triflusulfuron-Methyl Dissipation in Water and Soil. *Journal of Agricultural and Food Chemistry* **2000**, *48*, 3733–3737, https://doi.org/10.1021/jf9910943.
4. Zhu, C.; Zhang, C.; Zhang, M.; Wu, Y.; Zhang, Z.; Zhang, H. Degradation Characteristics and Soil Remediation of Thifensulfuron-Methyl by Immobilized Serratia Marcecens N80 Beads. *Environmental Technology & Innovation* **2021**, *24*, 102059, https://doi.org/10.1016/j.eti.2021.102059.

5. Xi, N.; Li, Y.; Xia, X. A Review of Pesticide Phototransformation on the Leaf Surface: Models, Mechanism, and Influencing Factors. *Chemosphere* **2022**, *308*, 136260, https://doi.org/10.1016/j.chemosphere.2022.136260.

6. Wang, Y.; Yu, W.; Chang, Z.; Gao, C.; Yang, Y.; Zhang, B.; Wang, Y.; Xing, B. Effects of Dissolved Organic Matter on the Adsorption of Norfloxacin on a Sandy Soil (Fraction) from the Yellow River of Northern China. *Science of The Total Environment* **2022**, *848*, 157495, https://doi.org/10.1016/j.scitotenv.2022.157495.

7. Ewis, D.; Ba-Abbad, M.M.; Benamor, A.; El-Naas, M.H. Adsorption of Organic Water Pollutants by Clays and Clay Minerals Composites: A Comprehensive Review. *Applied Clay Science* **2022**, *229*, 106686, https://doi.org/10.1016/j.clay.2022.106686.

8. Goh, P.S.; Ahmad, N.A.; Wong, T.W.; Yogarathinam, L.T.; Ismail, A.F. Membrane Technology for Pesticide Removal from Aquatic Environment: Status Quo and Way Forward. *Chemosphere* **2022**, *307*, 136018, https://doi.org/10.1016/j.chemosphere.2022.136018.

9. Jia, H.; Zhao, J.; Fan, X.; Dilimulati, K.; Wang, C. Photodegradation of Phenanthrene on Cation-Modified Clays under Visible Light. *Applied Catalysis B: Environmental* **2012**, *123–124*, 43–51, https://doi.org/10.1016/j.apcatb.2012.04.017.

10. Sturini, M.; Speltini, A.; Maraschi, F.; Profumo, A.; Pretali, L.; Fasani, E.; Albini, A. Sunlight-Induced Degradation of Soil-Adsorbed Veterinary Antimicrobials Marbofloxacin and Enrofloxacin. *Chemosphere* **2012**, *86*, 130–137, https://doi.org/10.1016/j.chemosphere.2011.09.053.

11. Wolters, A.; Steffens, M. Photodegradation of Antibiotics on Soil Surfaces: Laboratory Studies on Sulfadiazine in an Ozone-Controlled Environment. *Environ. Sci. Technol.* **2005**, *39*, 6071–6078, https://doi.org/10.1021/es048264z.

12. Barreca, S.; Orecchio, S.; Pace, A. The Effect of Montmorillonite Clay in Alginate Gel Beads for Polychlorinated Biphenyl Adsorption: Isothermal and Kinetic Studies. *Applied Clay Science* **2014**, *99*, 220–228, https://doi.org/10.1016/j.clay.2014.06.037.

13. Hu, M.; Hou, N.; Li, Y.; Liu, Y.; Zhang, H.; Zeng, D.; Tan, H. The Effect of Microplastics on Behaviors of Chiral Imidazolinone Herbicides in the Aquatic Environment: Residue, Degradation and Distribution. *Journal of Hazardous Materials* **2021**, *418*, 126176, https://doi.org/10.1016/j.jhazmat.2021.126176.

14. Ighalo, J.O.; Yap, P.-S.; Iwuozor, K.O.; Aniagor, C.O.; Liu, T.; Dulta, K.; Iwuchukwu, F.U.; Rangabhashiyam, S. Adsorption of Persistent Organic Pollutants (POPs) from the Aqueous Environment by Nano-Adsorbents: A Review. *Environmental Research* **2022**, *212*, 113123, https://doi.org/10.1016/j.envres.2022.113123.

15. Rafqah, S.; Wong-Wah-Chung, P.; Aamili, A.; Sarakha, M. Degradation of Metsulfuron Methyl by Heterogeneous Photocatalysis on TiO2 in Aqueous Suspensions: Kinetic and Analytical Studies. *Journal of Molecular Catalysis A: Chemical* **2005**, *237*, 50–59, https://doi.org/10.1016/j.molcata.2005.03.044.

16. Hofstetter, T.B.; Schwarzenbach, R.P.; Haderlein, S.B. Reactivity of Fe(II) Species Associated with Clay Minerals. *Environmental Science & Technology* **2003**, *37*, 519–528, https://doi.org/10.1021/es025955r.

17. Zhou, Z.; Zeng, Q.; Li, G.; Hu, D.; Xia, Q.; Dong, H. Oxidative Degradation of Commingled Trichloroethylene and 1,4-Dioxane by Hydroxyl Radicals Produced upon Oxygenation of a Reduced Clay Mineral. *Chemosphere* **2022**, *290*, 133265, https://doi.org/10.1016/j.chemosphere.2021.133265.

18. Chen, N.; Fang, G.; Liu, G.; Zhou, D.; Gao, J.; Gu, C. The Effects of Fe-Bearing Smectite Clays on OH Formation and Diethyl Phthalate Degradation with Polyphenols and H2O2. *Journal of Hazardous Materials* **2018**, *357*, 483–490, https://doi.org/10.1016/j.jhazmat.2018.06.030.

19. Bryliakov, K.P. Catalytic Asymmetric Oxygenations with the Environmentally Benign Oxidants H_2O_2 and O_2. *Chemical Reviews* **2017**, *117*, 11406–11459, https://doi.org/10.1021/acs.chemrev.7b00167.

20. Hou, X.; Huang, X.; Jia, F.; Ai, Z.; Zhao, J.; Zhang, L. Hydroxylamine Promoted Goethite Surface Fenton Degradation of Organic Pollutants. *Environmental Science & Technology* **2017**, *51*, 5118–5126, https://doi.org/10.1021/acs.est.6b05906.

21. Qin, Y.; Song, F.; Ai, Z.; Zhang, P.; Zhang, L. Protocatechuic Acid Promoted Alachlor Degradation in Fe(III)/H_2O_2 Fenton System. *Environmental Science & Technology* **2015**, *49*, 7948–7956, https://doi.org/10.1021/es506110w.

22. Chong, M.N.; Lei, S.; Jin, B.; Saint, C.; Chow, C.W.K. Optimisation of an Annular Photoreactor Process for Degradation of Congo Red Using a Newly Synthesized Titania Impregnated Kaolinite Nano-Photocatalyst. *Separation and Purification Technology* **2009**, *67*, 355–363, https://doi.org/10.1016/j.seppur.2009.04.001.

23. Chong, M.N.; Vimonses, V.; Lei, S.; Jin, B.; Chow, C.; Saint, C. Synthesis and Characterisation of Novel Titania Impregnated Kaolinite Nano-Photocatalyst. *Microporous and Mesoporous Materials* **2009**, *117*, 233–242, https://doi.org/10.1016/j.micromeso.2008.06.039.

24. Yuan, L.; Huang, D.; Guo, W.; Yang, Q.; Yu, J. TiO2/Montmorillonite Nanocomposite for Removal of Organic Pollutant. *Applied Clay Science* **2011**, *53*, 272–278, https://doi.org/10.1016/j.clay.2011.03.013.

25. Bouyarmane, H.; El Bekkali, C.; Labrag, J.; Es-saidi, I.; Bouhnik, O.; Abdelmoumen, H.; Laghzizil, A.; Nunzi, J.-M.; Robert, D. Photocatalytic Degradation of Emerging Antibiotic Pollutants in Waters by

TiO2/Hydroxyapatite Nanocomposite Materials. *Surfaces and Interfaces* **2021**, *24*, 101155, https://doi.org/10.1016/j.surfin.2021.101155.

26. Ronald, W.; G.W., B. The Crystal Structures of Pyrophyllite, 1Te, and of Its Dehydroxylate 1971, http://www.minsocam.org/ammin/AM57/AM57_732.pdf.

27. Young, R.A. Verification of the Triclinic Crystal Structure of Kaolinite. *Clays and Clay Minerals* **1988**, *36*, 225–232, https://doi.org/10.1346/CCMN.1988.0360303.

28. Delley, B. From Molecules to Solids with the DMol3 Approach. *The Journal of Chemical Physics* **2000**, *113*, 7756–7764, https://doi.org/10.1063/1.1316015.

29. *Materials Studio*; Accelrys Software Inc., San Diego, 2016.

30. Perdew, J.P.; Burke, K.; Ernzerhof, M. Generalized Gradient Approximation Made Simple. *Phys. Rev. Lett.* **1996**, *77*, 3865–3868, https://doi.org/10.1103/PhysRevLett.77.3865.

31. Gašparič, L.; Poberžnik, M.; Kokalj, A. DFT Study of Hydrogen Bonding between Metal Hydroxides and Organic Molecules Containing N, O, S, and P Heteroatoms: Clusters vs. Surfaces. *Chemical Physics* **2022**, *559*, 111539, https://doi.org/10.1016/j.chemphys.2022.111539.

32. Frenkel, D.; Smit, B. *Understanding Molecular Simulation: From Algorithms to Applications*; 2002; ISBN 9780080519982, https://www.sciencedirect.com/book/9780122673511/understanding-molecular-simulation.

33. Rappe, A.K.; Casewit, C.J.; Colwell, K.S.; Goddard, W.A.; Skiff, W.M. UFF, a Full Periodic Table Force Field for Molecular Mechanics and Molecular Dynamics Simulations. *J. Am. Chem. Soc.* **1992**, *114*, 10024–10035, https://doi.org/10.1021/ja00051a040.

34. Metropolis, N.; Rosenbluth, A.W.; Rosenbluth, M.N.; Teller, A.H.; Teller, E. Equation of State Calculations by Fast Computing Machines. *The Journal of Chemical Physics* **1953**, *21*, 1087–1092, https://doi.org/10.1063/1.1699114.

35. Ewald, P.P. Investigations of Crystals by Means of Roentgen Rays. *Ann. Phy* **1921**, *64*, 253-264. https://doi.org/10.1002/andp.19213690304.

36. Brooks, C.L.; Pettitt, B.M.; Karplus, M. Structural and Energetic Effects of Truncating Long Ranged Interactions in Ionic and Polar Fluids. *The Journal of Chemical Physics* **1985**, *83*, 5897–5908, https://doi.org/10.1063/1.449621.

37. Lee, S.G.; Choi, J.I.; Koh, W.; Jang, S.S. Adsorption of β-d-Glucose and Cellobiose on Kaolinite Surfaces: Density Functional Theory (DFT) Approach. *Applied Clay Science* **2013**, *71*, 73–81, https://doi.org/10.1016/j.clay.2012.11.002.

38. Wang, S.; Song, X.; Hao, C.; Gao, Z.; Chen, J.; Qiu, J. Elucidating Triplet-Sensitized Photolysis Mechanisms of Sulfadiazine and Metal Ions Effects by Quantum Chemical Calculations. *Chemosphere* **2015**, *122*, 62–69, https://doi.org/10.1016/j.chemosphere.2014.11.007.

39. Francisco-Márquez, M.; Soriano-Correa, C.; Sainz-Díaz, C.I. Adsorption of Sulfonamides on Phyllosilicate Surfaces by Molecular Modeling Calculations. *J. Phys. Chem. C* **2017**, *121*, 2905–2914, https://doi.org/10.1021/acs.jpcc.6b12467.

40. Borrego-Sánchez, A.; Carazo, E.; Aguzzi, C.; Viseras, C.; Sainz-Díaz, C.I. Biopharmaceutical Improvement of Praziquantel by Interaction with Montmorillonite and Sepiolite. *Applied Clay Science* **2018**, *160*, 173–179, https://doi.org/10.1016/j.clay.2017.12.024.

41. Rebitski, E.P.; Alcântara, A.C.S.; Darder, M.; Cansian, R.L.; Gómez-Hortigüela, L.; Pergher, S.B.C. Functional Carboxymethylcellulose/Zein Bionanocomposite Films Based on Neomycin Supported on Sepiolite or Montmorillonite Clays. *ACS Omega* **2018**, *3*, 13538–13550, https://doi.org/10.1021/acsomega.8b01026.

42. Meirelles, L.; Carazo, E.; Borrego-Sánchez, A.; Barbosa, R.; Moura, T.; Aguzzi, C.; Sainz-Diaz, C.I.; Viseras, C.; Raffin, F. Design and Characterization of a Tuberculostatic Hybrid Based on Interaction of Ethambutol with a Raw Palygorskite. *Applied Clay Science* **2019**, *181*, 105213, https://doi.org/10.1016/j.clay.2019.105213.

43. Minakata, D.; Crittenden, J. Linear Free Energy Relationships between Aqueous Phase Hydroxyl Radical Reaction Rate Constants and Free Energy of Activation. *Environ. Sci. Technol.* **2011**, *45*, 3479–3486, https://doi.org/10.1021/es1020313.

44. Nayebzadeh, M.; Vahedpour, M.; Shiroudi, A.; Rius-Bartra, J.M. Kinetics and Oxidation Mechanism of Pyrene Initiated by Hydroxyl Radical. A Theoretical Investigation. *Chemical Physics* **2020**, *528*, 110522, https://doi.org/10.1016/j.chemphys.2019.110522.

45. Xiao, R.; Noerpel, M.; Ling Luk, H.; Wei, Z.; Spinney, R. Thermodynamic and Kinetic Study of Ibuprofen with Hydroxyl Radical: A Density Functional Theory Approach. *Int. J. Quantum Chem.* **2014**, *114*, 74–83, https://doi.org/10.1002/qua.24518.

46. Yang, Z.; Luo, S.; Wei, Z.; Ye, T.; Spinney, R.; Chen, D.; Xiao, R. Rate Constants of Hydroxyl Radical Oxidation of Polychlorinated Biphenyls in the Gas Phase: A Single−descriptor Based QSAR and DFT Study. *Environmental Pollution* **2016**, *211*, 157–164, https://doi.org/10.1016/j.envpol.2015.12.044.

47. Yang, J.; Lv, G.; Li, T.; Sun, S.; Sun, X. Theoretical Insight into the Degradation of Diclofenac by Hydroxyl and Sulfate Radicals in Aqueous-Phase: Mechanisms, Kinetics and Eco-Toxicity. *Journal of Environmental Chemical Engineering* **2022**, *10*, 108311, https://doi.org/10.1016/j.jece.2022.108311.

48. Frisch, M.J. et al *GAUSSIAN 09, Revision E. 01, Gaussian Inc., Wallingford*; 2009, https://www.scirp.org/(S(351jmbntvnsjt1aadkposzje))/reference/ReferencesPapers.aspx?ReferenceID=1399207.

49. Becke, A.D. Density-functional Thermochemistry. III. The Role of Exact Exchange. *The Journal of Chemical Physics* **1993**, *98*, 5648–5652, https://doi.org/10.1063/1.464913.

50. Lee, C.; Yang, W.; Parr, R.G. Development of the Colle-Salvetti Correlation-Energy Formula into a Functional of the Electron Density. *Phys. Rev. B* **1988**, *37*, 785–789, https://doi.org/10.1103/PhysRevB.37.785.

51. Reed, A.E.; Curtiss, L.A.; Weinhold, F. Intermolecular Interactions from a Natural Bond Orbital, Donor-Acceptor Viewpoint. *Chem. Rev.* **1988**, *88*, 899–926, https://doi.org/10.1021/cr00088a005.

52. Geerlings, P.; De Proft, F.; Langenaeker, W. Conceptual Density Functional Theory. *Chem. Rev.* **2003**, *103*, 1793–1874, https://doi.org/10.1021/cr990029p.

53. Oláh, J.; Van Alsenoy, C.; Sannigrahi, A.B. Condensed Fukui Functions Derived from Stockholder Charges: Assessment of Their Performance as Local Reactivity Descriptors. *J. Phys. Chem. A* **2002**, *106*, 3885–3890, https://doi.org/10.1021/jp014039h.

54. Torrent-Sucarrat, M.; De Proft, F.; Geerlings, P. Stiffness and Raman Intensity: A Conceptual and Computational DFT Study. *J. Phys. Chem. A* **2005**, *109*, 6071–6076, https://doi.org/10.1021/jp044150y.

55. Roy, R.K.; Krishnamurti, S.; Geerlings, P.; Pal, S. Local Softness and Hardness Based Reactivity Descriptors for Predicting Intra- and Intermolecular Reactivity Sequences: Carbonyl Compounds. *J. Phys. Chem. A* **1998**, *102*, 3746–3755, https://doi.org/10.1021/jp973450v.

56. Yang, W.; Parr, R.G. Hardness, Softness, and the Fukui Function in the Electronic Theory of Metals and Catalysis. *Proceedings of the National Academy of Sciences* **1985**, *82*, 6723–6726, https://doi.org/10.1073/pnas.82.20.6723.

57. Chaudret, R.; de Courcy, B.; Contreras-García, J.; Gloaguen, E.; Zehnacker-Rentien, A.; Mons, M.; Piquemal, J.-P. Unraveling Non-Covalent Interactions within Flexible Biomolecules: From Electron Density Topology to Gas Phase Spectroscopy. *Phys. Chem. Chem. Phys.* **2014**, *16*, 9876, https://doi.org/10.1039/c3cp52774c.

58. Lu, T.; Chen, F. Multiwfn: A Multifunctional Wavefunction Analyzer. *J. Comput. Chem.* **2012**, *33*, 580–592, https://doi.org/10.1002/jcc.22885.

59. Humphrey, W.; Dalke, A.; Schulten, K. VMD: Visual Molecular Dynamics. *Journal of Molecular Graphics* **1996**, *14*, 33–38, https://doi.org/10.1016/0263-7855(96)00018-5.

60. Bhattacharyya, K.G.; Gupta, S.S. Influence of Acid Activation on Adsorption of Ni(II) and Cu(II) on Kaolinite and Montmorillonite: Kinetic and Thermodynamic Study. *Chemical Engineering Journal* **2008**, *136*, 1–13, https://doi.org/10.1016/j.cej.2007.03.005.

61. Liu, Y.-L.; Walker, H.W.; Lenhart, J.J. Adsorption of Microcystin-LR onto Kaolinite, Illite and Montmorillonite. *Chemosphere* **2019**, *220*, 696–705, https://doi.org/10.1016/j.chemosphere.2018.12.137.

62. Caselli, M.; Ponterini, G.; Vignali, M. Irradiation-Wavelength Dependent Photochemistry of the Bichromophoric Sulfonylurea Chlorsulfuron. *Journal of Photochemistry and Photobiology A: Chemistry* **2001**, *138*, 129–137, https://doi.org/10.1016/S1010-6030(00)00392-0.

63. Vulliet, E.; Emmelin, C.; Grenier-Loustallot, M.F.; Païssé, O.; Chovelon, J.M. Simulated Sunlight-Induced Photodegradations of Triasulfuron and Cinosulfuron in Aqueous Solutions. *J. Agric. Food Chem.* **2002**, *50*, 1081–1088, https://doi.org/10.1021/jf010948s.

64. Vulliet, E.; Emmelin, C.; Chovelon, J.-M. Influence of PH and Irradiation Wavelength on the Photochemical Degradation of Sulfonylureas. *Journal of Photochemistry and Photobiology A: Chemistry* **2004**, *163*, 69–75, https://doi.org/10.1016/S1010-6030(03)00434-9.

65. Rafqah, S.; Chung, P.W.-W.; Forano, C.; Sarakha, M. Photocatalytic Degradation of Metsulfuron Methyl in Aqueous Solution by Decatungstate Anions. *Journal of Photochemistry and Photobiology A: Chemistry* **2008**, *199*, 297–302, https://doi.org/10.1016/j.jphotochem.2008.06.012.

66. Bottaro, M.; Frascarolo, P.; Gosetti, F.; Mazzucco, E.; Gianotti, V.; Polati, S.; Pollici, E.; Piacentini, L.; Pavese, G.; Gennaro, M.C. Hydrolytic and Photoinduced Degradation of Tribenuron Methyl Studied by HPLC-DAD-MS/MS. *J Am Soc Mass Spectrom* **2008**, *19*, 1221–1229, https://doi.org/10.1016/j.jasms.2008.05.009.

67. Samanta, S.; Kole, R.K.; Chowdhury, A. Photodegradation of Metsulfuron Methyl in Aqueous Solution. *Chemosphere* **1999**, *39*, 873–879, https://doi.org/10.1016/S0045-6535(99)00029-6.

68. Gournis, D.; Karakassides, M.A.; Petridis, D. Formation of Hydroxyl Radicals Catalyzed by Clay Surfaces. *Physics and Chemistry of Minerals* **2002**, *29*, 155–158, https://doi.org/10.1007/s002690100215.

69. Menager, M.; Sarakha, M. Simulated Solar Light Phototransformation of Organophosphorus Azinphos Methyl at the Surface of Clays and Goethite. *Environ. Sci. Technol.* **2013**, *47*, 765–772, https://doi.org/10.1021/es301866f.

70. Ioffe, M.; Kundu, S.; Perez-Lapid, N.; Radian, A. Heterogeneous Fenton Catalyst Based on Clay Decorated with Nano-Sized Amorphous Iron Oxides Prevents Oxidant Scavenging through Surface Complexation. *Chemical Engineering Journal* **2022**, *433*, 134609, https://doi.org/10.1016/j.cej.2022.134609.

71. Chen, N.; Geng, M.; Huang, D.; Tan, M.; Li, Z.; Liu, G.; Zhu, C.; Fang, G.; Zhou, D. Hydroxyl Radical Formation during Oxygen-Mediated Oxidation of Ferrous Iron on Mineral Surface: Dependence on Mineral Identity. *Journal of Hazardous Materials* **2022**, *434*, 128861, https://doi.org/10.1016/j.jhazmat.2022.128861.

72. Aziz, S.; Dumas, S.; El Azzouzi, M.; Sarakha, M.; Chovelon, J.-M. Photophysical and Photochemical Studies of Thifensulfuron-Methyl Herbicide in Aqueous Solution. *Journal of Photochemistry and Photobiology A: Chemistry* **2010**, *209*, 210–218, https://doi.org/10.1016/j.jphotochem.2009.11.017.

73. Wiberg, K.B. Application of the Pople-Santry-Segal CNDO Method to the Cyclopropylcarbinyl and Cyclobutyl Cation and to Bicyclobutane. *Tetrahedron* **1968**, *24*, 1083–1096, https://doi.org/10.1016/0040-4020(68)88057-3.

74. Monti, S.; Sortino, S.; Fasani, E.; Albini, A. Multifaceted Photoreactivity of 6-Fluoro-7-Aminoquinolones from the Lowest Excited States in Aqueous Media: A Study by Nanosecond and Picosecond Spectroscopic Techniques. *Chemistry* **2001**, *7*, 2185–2196, https://doi.org/10.1002/1521-3765(20010518)7:10<2185::aid-chem2185>3.0.co;2-u.

75. Wang, S.; Song, X.; Hao, C.; Gao, Z.; Chen, J.; Qiu, J. Elucidating Triplet-Sensitized Photolysis Mechanisms of Sulfadiazine and Metal Ions Effects by Quantum Chemical Calculations. *Chemosphere* **2015**, *122*, 62–69, https://doi.org/10.1016/j.chemosphere.2014.11.007.